Activity-Based Imaging of Lipid Environments Targeted by Peroxynitrite in Biomimetic Vesicles and Live Cells

Bryan Gutierrez [1], Huseyin Erguven[1], M. Rhia L. Stone[1], Tushar Aggarwal[1], and Enver Cagri Izgu[1,2,3] *

(1) Department of Chemistry and Chemical Biology, Rutgers University, New Brunswick, NJ 08854, USA

(2) Cancer Institute of New Jersey, Rutgers University, New Brunswick, NJ 08901, USA

(3) Rutgers Center for Lipid Research, New Jersey Institute for Food, Nutrition, and Health, Rutgers University, New Brunswick, NJ 08901, USA

*Corresponding author: Izgu, E. C. (ec.izgu@rutgers.edu)

ABSTRACT

Peroxynitrite ($ONOO^-$), a redox-active species generated under nitrosative stress conditions, can promote oxidative damage of lipids. Herein, we report the development and multifaceted utilization of a novel, activity-based phospholipid probe, **PLP-ONOO$^-$**, for imaging lipid environments that are targeted by $ONOO^-$ in biomimetic and biological systems. Using **PLP-ONOO$^-$** and the natural lipid 1-palmitoyl-2-oleoyl-*sn*-glycero-3-phosphocholine, we built synthetic protocell membranes in the form of giant vesicles (GVs). These GVs responded to $ONOO^-$ by lighting up and displayed excellent selectivity against other redox-active species, introducing an unprecedented function to biomimetic membrane architectures. Live HeLa cells containing **PLP-ONOO$^-$** were investigated under cellular nitrosative stress induced by either external administration of peroxynitrite or endogenous stimulation with interferon-γ / lipopolysaccharide / phorbol myristate acetate. Both conditions enhanced the coumarin fluorescence within cells, providing insight into intracellular lipid environments potentially prone to peroxynitrite-mediated oxidative damage. This work offers a chemical reactivity-dependent function for synthetic vesicles and opens a possibility for investigating nitrosative stress at subcellular levels.

INTRODUCTION

Lipids are dynamic and chemically diverse biomolecular components of cells, playing essential roles in cellular growth, division, defense, waste disposal, energy storage, and communication.[1,2] Unsaturated lipids, like proteins,[3] nucleic acids,[4,5] and transition-metals,[6] are potential targets of redox-active species.[7,8] Reactions involving a change in atomic oxidation state – redox reactions – form a fundamental basis of cellular chemistry in all known life forms.[9,10] The concentrations of reactive nitrogen and oxygen (RNS and ROS) and redox mechanisms are tightly controlled in order to maintain cell homeostasis and minimize side reactions causing cell damage.[11–13] One redox-active species of particular interest concerning damage to lipids is peroxynitrite ($ONOO^-$), a highly potent member of both RNS and ROS families. Physiological production of $ONOO^-$ occurs through the diffusion-controlled reaction between nitric oxide (NO) and superoxide ($O_2^{\bullet -}$).[3] The physiologically normal concentration of $ONOO^-$ can be in the single-digit μM range, while it reaches up to 100 μM under dysregulated conditions.[13,14] Notably, peroxynitrite diffuses to longer distances than many other redox molecules and may be taken up by cells through anion transporters.[15] As a specific comparison, the diffusion distance of hydroxyl radical ($^{\bullet}OH$) is ~6 nm,[16] roughly the size of a small protein, whereas that of $ONOO^-$ is estimated to be in the range of 10–100 μm,[17] corresponding to 1–2 mammalian cell diameters.

The mechanism of peroxynitrite-mediated lipid damage has been proposed to involve hydrogen-abstraction from unsaturated lipids, such as linolenic acid, arachidonic acid, generating carbon-centered lipid radicals.[8,18] These radicals can react with nearby unsaturated lipids and are typically trapped by molecular oxygen (O_2) to form lipid peroxides. Accumulation of these lipid peroxides and their lipid/protein degradation products have been linked to protein aggregation in the nerves and subsequent development of neurodegenerative disorders, such as Parkinson's,[19,20] and glioma.[21–23] Furthermore, peroxynitrite-induced lipid oxidation has been linked to the progression of cardiovascular diseases like diabetic cardiomyopathy.[24]

As peroxynitrite is emerging to be a key species involved in cellular stress and different forms of pathophysiologies,[13,25,26] developing molecular tools to investigate its impact on biomolecules, including lipids, is of fundamental importance. Although the chemical reactivity of redox-active species is widely studied, their point of interaction with lipids *in vitro* or *in cellulo* has been underexplored. Fluorescent probes sensitive to intracellular peroxynitrite are available,[27–36] however, a molecular platform that allows imaging of lipid environments that are targeted by peroxynitrite in biomimetic systems or live cells has yet to be realized.

Herein, we report the development and multifaceted utilization of an activity-based phospholipid probe, **PLP-ONOO$^-$** (Scheme 1), that can detect ONOO$^-$ in proximity to lipid environments in both biomimetic and biological systems. Using this designer lipid and 1-palmitoyl-2-oleoyl-*sn*-glycero-3-phosphocholine (POPC), we built synthetic mimics of protocell membranes in the form of giant vesicles (GVs). These GVs responded to ONOO$^-$ by lighting up at the membrane, with the vesicle structures remaining intact. Additionally, they displayed excellent selectivity against other redox-active species, ushering in a previously unknown function to biomimetic membrane designs. We then introduced **PLP-ONOO$^-$** into a model mammalian cell line (HeLa) to establish its cellular uptake. Liposomal particles prepared from **PLP-ONOO$^-$** and cationic and zwitterionic lipids were successfully taken up by HeLa cells. Nitrosative stress, induced through either external administration of ONOO$^-$ or endogenous stimulation with interferon-γ (IFN-γ) / lipopolysaccharide (LPS) / phorbol myristate acetate (PMA), led to enhanced fluorescence of intracellular regions of lipid clusters. Collectively, this study offers a new molecular platform for the development of lipid-based self-assemblies capable of selectively sensing a chemical cue. In addition, our methodology enables investigation into the reactivity of ONOO$^-$ within intracellular lipid environments under nitrosative stress.

RESULTS AND DISCUSSION

The peroxynitrite-sensing phospholipid and its non-amphiphilic model were constructed through a modular chemical design. We developed a concise synthetic route for the peroxynitrite-sensing phospholipid, **PLP-ONOO$^-$** (Scheme 1), which include *p*-(4,4,4-trifluoro-3-oxobutyl)phenyl group as the peroxynitrite-reactive moiety,[27] 3-triazole-coumarin as the fluorogenic segment, and dipalmitoylphosphatidylcholine (DPPC) as the amphiphilic molecular framework. In addition, to facilitate investigations of the peroxynitrite-mediated florescence activation mechanism and fidelity, we synthesized **TEGP-ONOO$^-$**, a non-amphiphilic analog of **PLP-ONOO$^-$**. Both probes contain an identical peroxynitrite-reactive motif and coumarin core. However, investigating the mechanism and fidelity of peroxynitrite sensing by spectroscopic and spectrophotometric analyses is more feasible with **TEGP-ONOO$^-$**, as it contains a triethylene glycol (TEG) group instead of a hydrocarbon tail and thus exists in non-aggregated state in aqueous media. For both of these probes, the *p*-(4,4,4-trifluoro-3-oxobutyl)phenyl and 3-triazole-7-hydroxycoumarin groups were connected through a carbonate linkage. We reasoned that the carbonate linkage could mask 7-*O* of the coumarin, diminishing its fluorescence intensity. In the

presence of $ONOO^-$, the *p*-(4,4,4-trifluoro-3-oxobutyl)phenyl moiety would undergo an oxidative elimination cascade, resulting in decarboxylative uncaging of the coumarin motif.

Probes **TEGP-ONOO**$^-$ and **PLP-ONOO**$^-$ were synthesized through convergent routes in which the longest linear sequence required three chemical steps. First, 1,1,1-trifluoro-4-(4-hydroxyphenyl)butan-2-one (**1**) was converted to its chloroformate using triphosgene and successively connected with 3-azido-7-hydroxycoumarin (**2**) to furnish the carbonate **3** in 60% isolated yield over two steps. This azido carbonate compound served as a common intermediate towards both **TEGP-ONOO**$^-$ and **PLP-ONOO**$^-$: Each probe was obtained from **3** via copper-catalyzed azide alkyne cycloaddition reaction with its respective conjugation partner, the propargylated *rac*-DPPC **4** or propargyl-TEG-OH **5**. To obtain **4**, we converted 1,2-dipalmitoyl-*rac*-glycerol to its cyclic phosphate triester using ethylene chlorophosphite and opened the subsequent phosphate triester ring by the nucleophilic addition of 3-dimethylamino-1-propyne (see Supplementary Information for details). Both **TEGP-ONOO**$^-$ and **PLP-ONOO**$^-$ undergoes oxidative decarboxylation to form their respective uncaged coumarins **TEGP*** and **PLP***. The anionic form of the coumarin should exhibit a stronger fluorescence compared to its neutral analog. In accordance, we found the pK_a of the model coumarin **TEGP*** as 7.1 ± 0.1 using UV-Vis spectrophotometric measurements (Figure S1). The uncaging of these coumarins were tested *in vitro* at alkaline conditions (pH ~7.5–8.5), which allowed peroxynitrite to have a half-life longer than 1 s (Figure S2). At this pH, a substantial population of the coumarin moiety is expected to be in the aryloxide form.

Next, we assessed the impact of coumarin caging and uncaging on molecule fluorogenicity by measuring the relative fluorescence quantum yield ($\Phi_{F\mathit{rel}}$) of the probes (**TEGP-ONOO**$^-$ and **PLP-ONOO**$^-$) and their oxidative decarboxylation products (**TEGP*** and **PLP***). Toward this end, we used coumarin 343 as the standard, whose absolute fluorescence quantum yield (Φ_F) is 0.65 in ethanol.[37] Relative to this standard and under the identical solvent condition, $\Phi_{F\mathit{rel}\text{-}\mathbf{TEGP^*}}$ and $\Phi_{F\mathit{rel}\text{-}\mathbf{PLP^*}}$ were measured as 0.67 and 0.64, respectively. As expected, caging the coumarin with the oxobutyl phenyl carbonate moiety decreased the fluorescence quantum yield significantly. The $\Phi_{F\mathit{rel}\text{-}\mathbf{TEGP\text{-}ONOO^-}}$ and $\Phi_{F\mathit{rel}\text{-}\mathbf{PLP\text{-}ONOO^-}}$ were determined to be 0.08 and 0.09, respectively, indicating a stark difference in fluorogenicity between the free and caged coumarin designs.

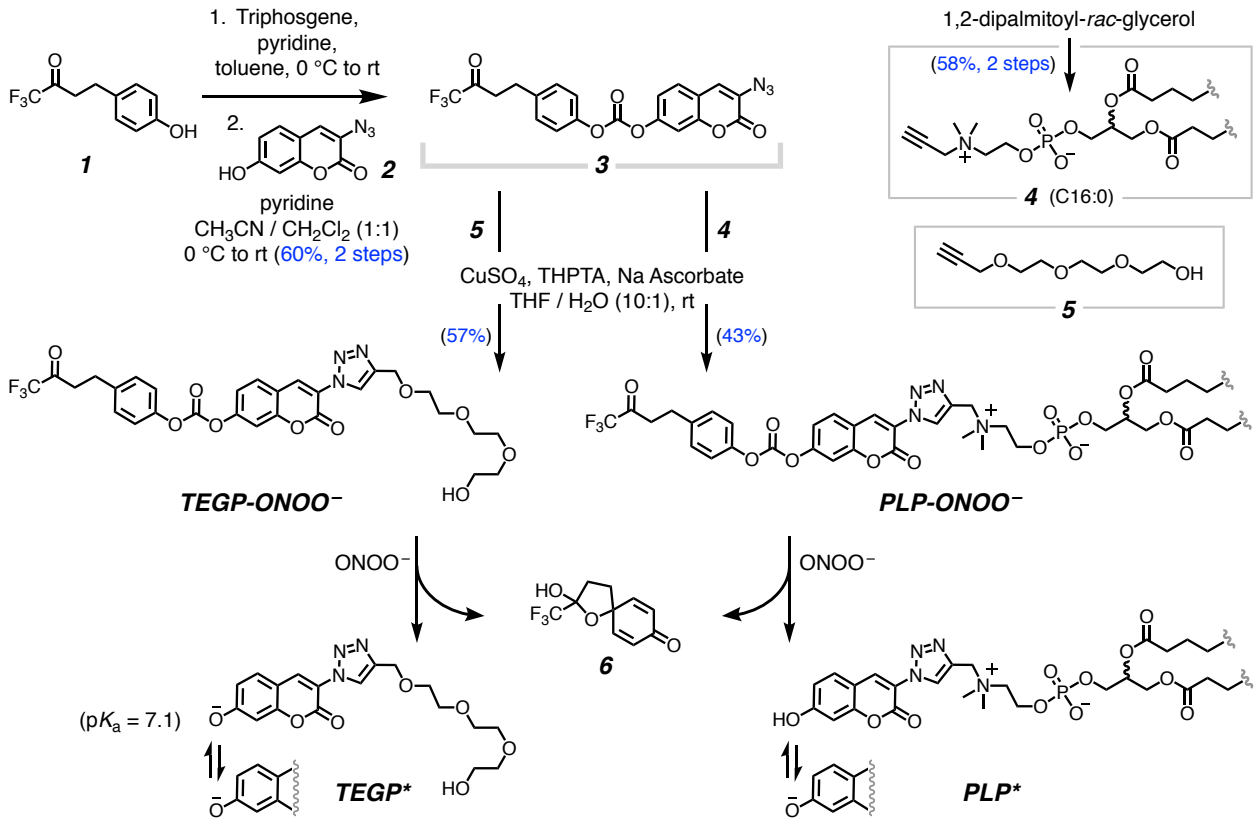

Scheme 1. The chemical synthesis and peroxynitrite-mediate oxidative conversion of the model probe **TEGP-ONOO⁻** and phospholipid probe **PLP-ONOO⁻**. THPTA: tris(3-hydroxypropyltriazolyl-methyl)amine. Φ_{Frel} denotes relative fluorescence quantum yield.

Sensing occurs via oxidative uncaging of the coumarin motif and is specific to peroxynitrite. Mass spectrometry analysis of the crude mixture of **TEGP-ONOO⁻** and peroxynitrite indicated the formation of the uncaged coumarin **TEGP*** and the oxa-spiro[4,5] decenone **6** as the major reaction products (Figure S3).

The response rate and magnitude of **TEGP-ONOO⁻** against ONOO⁻ was evaluated by measuring the relative fluorescence intensities of samples containing **TEGP-ONOO⁻** and **TEGP*** (positive control) at 405 nm excitation (Figure 1A). These samples, prepared in Tris buffer (50 mM, pH 7.5), were measured over 60 minutes of incubation with and without ONOO⁻. Peroxynitrite production rate in cells have been reported to vary from 0.1–1 μM/min to 100 μM/min.[13,38] In light of these findings, and in agreement with the previously established assay conditions,[29] we reasoned that the administration of 600 μM of peroxynitrite into a pH 7.5 medium would fall within the representative peroxynitrite concentration range of ~10–20 μM/min. In accordance, the samples tested here were exposed to 600 μM of peroxynitrite to maintain a steady level of effective peroxynitrite throughout the measurements. Upon addition of

peroxynitrite, the sample containing **TEGP-ONOO⁻** exhibited a rapid increase in fluorescence, reaching 3-fold higher fluorescence compared to the sample untreated with peroxynitrite (Figure 1A). The difference in fluorescence between the peroxynitrite-treated and untreated samples reached up to 5-fold within 60 minutes. During this time period, the relative fluorescence intensity of the sample containing **TEGP-ONOO⁻** became ~85% of that of the sample containing the uncaged analog **TEGP*** (positive control). This trend of increasing fluorescence output was mirrored in the level of conversion of **TEGP-ONOO⁻** into **TEGP*** based on UV-Vis spectrophotometric measurements (Figure S4).

The peroxynitrite-specificity of the probe design was assessed by subjecting **TEGP-ONOO⁻** to other redox-active species, including NO, hydrogen peroxide (H_2O_2), $^{\bullet}OH$, singlet oxygen ($^1O_2$), and superoxide radical ($O_2^{\bullet -}$) (Figure 1B). Change in fluorescence intensity following excitation at 405 nm was measured over 60 minutes of incubation of **TEGP-ONOO⁻** with each species and presented based on the signal-to-background ratio F/F_0, where F and F_0 are defined as the fluorescence with and without the analyte. In the absence of a redox-active species, F/F_0 for **TEGP-ONOO⁻** increased only 13% (F/F_0 = 1.13) over 60 minutes. Treatment of **TEGP-ONOO⁻** with $ONOO^-$ gave rise to ~570% increase in fluorescence (F/F_0 = 6.69).

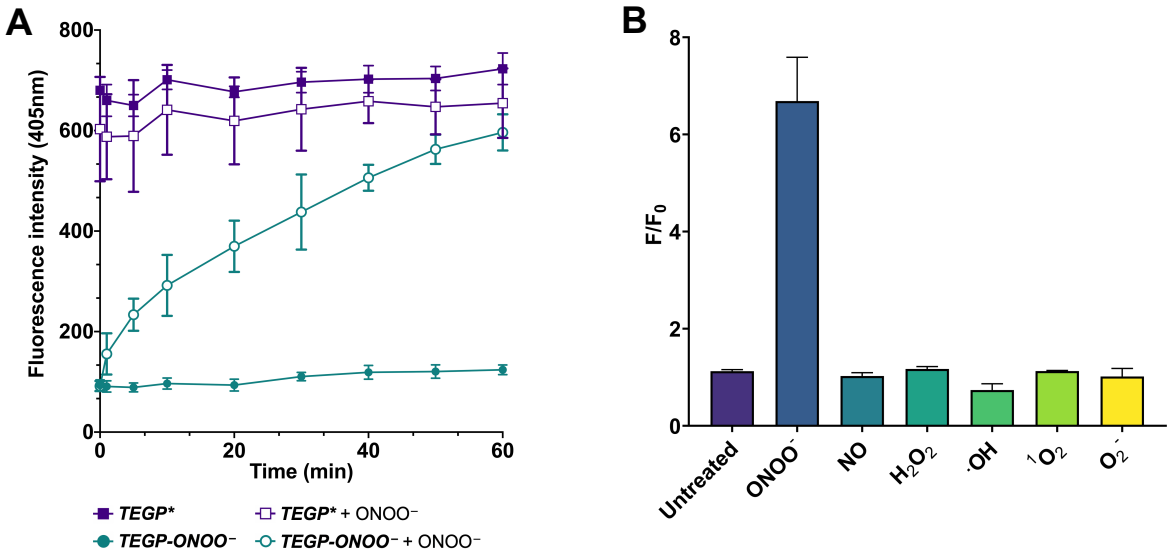

Figure 1. A. The time-dependent change in relative fluorescence intensities for probe **TEGP-ONOO⁻** (1 μM) and compound **TEGP*** (1 μM) in Tris (50 mM, pH 7.5) upon addition of $ONOO^-$ (600 μM). Error bars represent standard deviation, n = 3. **B.** Relative fluorescence intensity (F) with respect to the background fluorescence intensity (F_0) of **TEGP-ONOO⁻** in the absence or presence of redox-active species. Probe **TEGP-ONOO⁻** (1 μM) was dissolved in Tris buffer (50 mM, pH 7.5) and subjected to RNS and ROS (600 μM): $ONOO^-$, NO, H_2O_2, •OH, $^1O_2$, and O_2^-. Data represent F/F_0 measurements for samples incubated for 60 min. Plate reader was set to excitation at 405 nm and emission at 475 nm. Error bars represent standard deviation, n = 3.

Notably, incubating **TEGP-ONOO$^-$** with species other than $ONOO^-$ resulted in only negligible levels of change in fluorescence. NO, a free radical RNS that serves as a signaling molecule in cells, had essentially no effect on fluorescence intensity (F/F_0 = 1.03). The most significant fluorescence enhancement was observed for H_2O_2, with a fluorescence intensity 16% stronger than that of the background (F/F_0 = 1.16). These results indicate that the relative fluorescence enhancement of **TEGP-ONOO$^-$** is nearly 36-fold for $ONOO^-$ compared to the other RNS and ROS tested in this study.

Giant vesicles respond to peroxynitrite by lighting up at the membrane. In most biomimetic systems that rely on compartmentalization,[39] physical membrane boundaries are comprised of self-assembled lipids.[40] We studied the chemical reactivity and compartmentalization properties of **PLP-ONOO$^-$** as a component of phospholipid-based GVs (Figure 2A). These lipid self-assemblies (1–30 μm in diameter) have dimensional properties relevant to those of mammalian cells (10–100 μm), display physical characteristics feasible for confocal fluorescence imaging, and are utilized for bottom-up construction of biomimetic systems.[41–43] We produced GVs (both unilamellar and multilamellar) from POPC and **PLP-ONOO$^-$** (~99:1 molar ratio) using electroformation[44] (Figure S5). To label vesicle membranes, we employed 1,2-dioleoyl-*sn*-glycero-3-phosphoethanolamine-*N*-(lissamine rhodamine B sulfonyl) (18:1 Liss-Rhod PE) in 0.05 mol percent of the total lipid composition. Sucrose solution (400 mM) was used to hydrate the lipid films. A high solute concentration of sucrose facilitated the formation and stabilization of GV. Following electroformation, solutions of GVs were used within 24 hours. Vesicle size distribution was analyzed by dynamic light scattering (DLS), confirming the presence of GVs. DLS analysis showed that 91% of vesicles had diameters ranging from ~5 to 20 μm, with 48% had an average size of 5 μm in diameter (Figure S6). GVs were then imaged using fluorescence confocal microscopy. The vesicles were treated with the redox-active species, then mounted directly onto a microscope slide. Although significant vesicle motility was observed, the population density was sufficiently high to locate some static vesicles. Addition of peroxynitrite (100 μM final concentration) into mixture of GVs led to a substantial increase in membrane fluorescence at 405 nm excitation (Figure 2B), which was consistent with the observations of probe **TEGP-ONOO$^-$** in the vesicle-free reaction medium (Figure 1B). Notably, phospholipid **PLP-ONOO$^-$** makes the redox-sensing function of GVs highly selective towards $ONOO^-$. Incubation (5 min) with other redox-active species, including NO, H_2O_2, $^{\bullet}OH$, $^1O_2$, and $O_2^{\bullet -}$, resulted in essentially no fluorescence generation following excitation at 405 nm (Figure 2C).

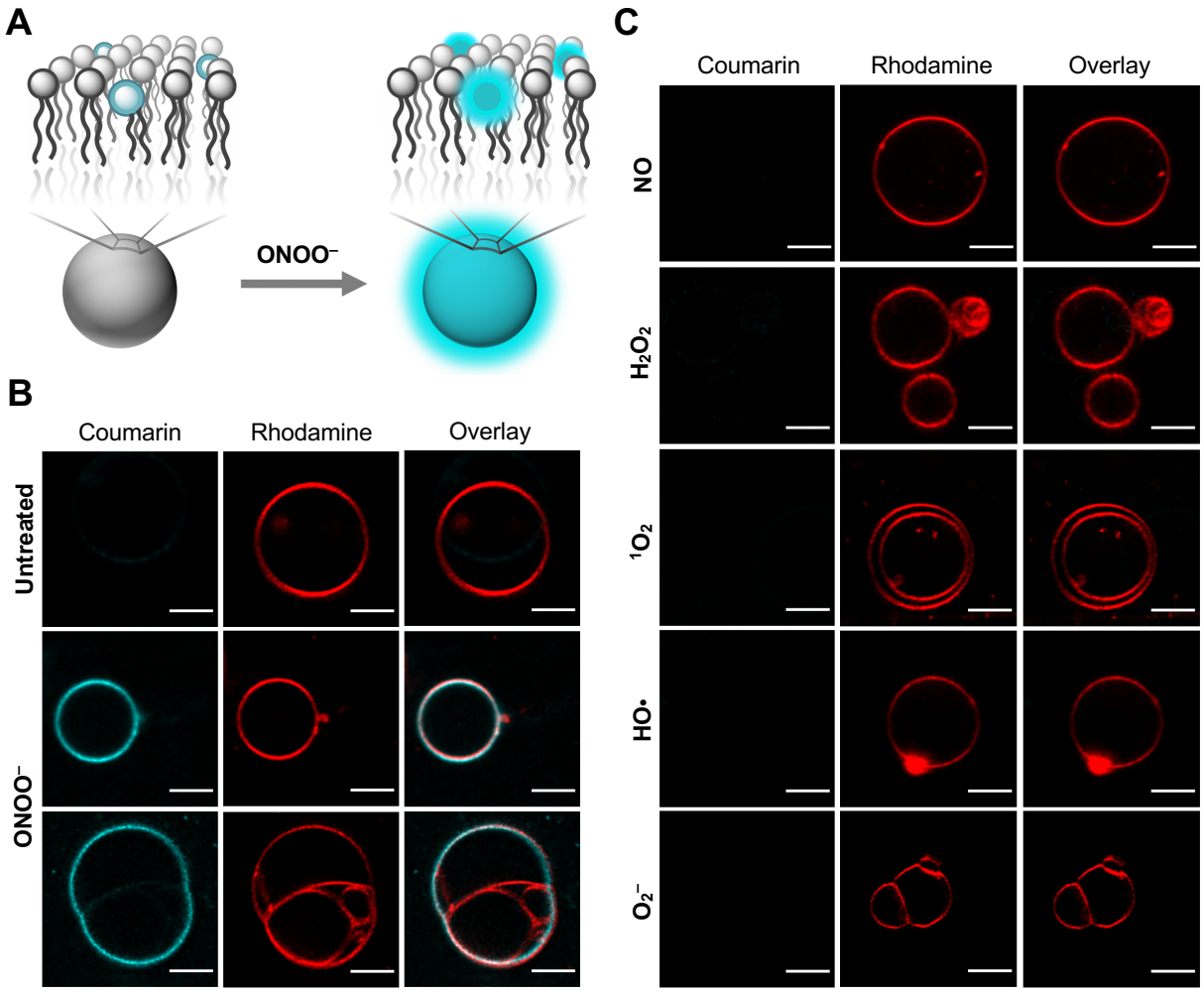

Figure 2. A. Functional protocell membrane mimics that sense peroxynitrite. **B.** Confocal images acquired for untreated (top panel) and peroxynitrite-treated (middle and bottom panels) giant vesicles (GVs). **C.** Confocal images acquired for GVs treated with other RNS and ROS. **B-C.** Vesicles were prepared from POPC (98.5%, molar ratio) and **PLP-ONOO⁻** (1%) via electroformation. Liss-Rhod PE dye (red, 560 nm excitation) was used to label vesicle membranes. This dye, which constituted 0.5% of the lipid composition, was not displayed in panel **A** for simplicity. In the absence of peroxynitrite or in the presence of other RNS or ROS (100 μM), vesicles emit minimal fluorescence at the coumarin channel (405 nm excitation). Vesicles are activated to emit strong fluorescence when peroxynitrite (100 μM) is present. Fluorescence images (coumarin, rhodamine, and a merge of both channels) are shown for each field of view to demonstrate the localization of the fluorescent phospholipid **PLP***, generated by peroxynitrite *in-situ*, with respect to the vesicle membranes. Scale bar = 5 μm.

PLP-ONOO⁻ allows imaging of intracellular lipid microenvironments targeted by peroxynitrite. With the utility of the lipid probe proven in synthetic protocell membranes, we sought to incorporate **PLP-ONOO⁻** into living HeLa cells (Figure 3A). To this end, liposomes (~100 nm in diameter) of **PLP-ONOO⁻**, Liss-Rhod PE, 1,2-di-*O*-octadecenyl-3-trimethylammonium propane (DOTMA), and 1,2-dioleoyl-*sn*-glycero-3-phosphoethanolamine

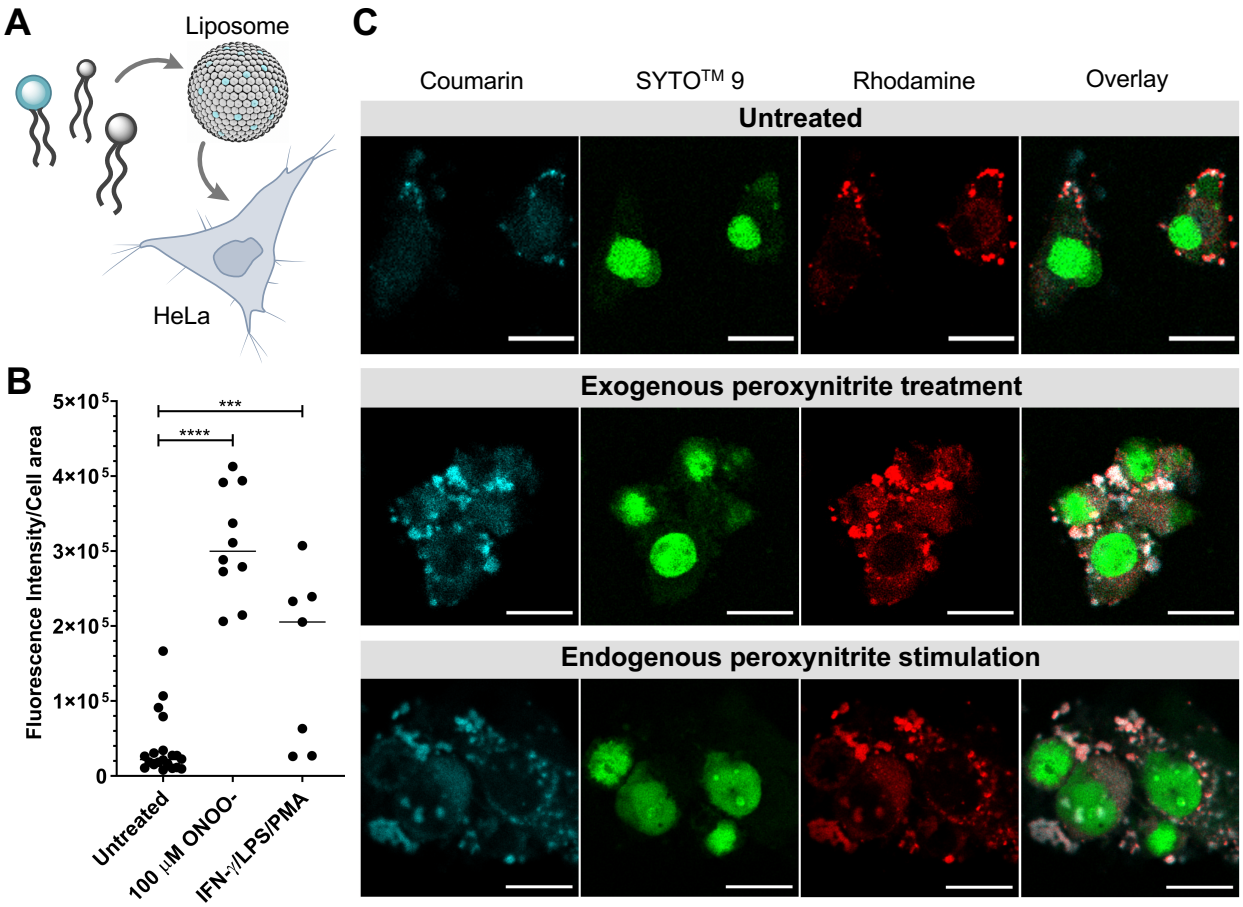

Figure 3. A. The strategy of liposomal uptake of **PLP-ONOO⁻** by HeLa cells. **B.** Imaging of intracellular lipid microenvironments impacted by peroxynitrite. Cells were seeded into microscope glass bottomed dishes, then incubated overnight with 50 μM liposomes containing Liss-Rhod PE (0.5% molar ratio), **PLP-ONOO⁻** (4.5%), DOTMA (47.5%) and DOPE (47.5%). Cells were then stained with SYTO™ 9 (488 nm excitation, nucleic acid stain) prior to imaging. Exogenous peroxynitrite was added at the microscope (final concentration 100 μM, in HBSS), whereas IFN-γ / LPS / PMA stimulation was carried out prior to imaging. **C.** Quantitative analysis of cellular fluorescence based on the peroxynitrite treatment. The quantification was carried out using Fiji by selecting cells with the polygon tool and extracting the total integrated fluorescence and cell size. Fluorescence divided by cell size (in μm) was then plotted, and statistical analyses were carried out by unpaired t-test in GraphPad Prism; ***: $p > 0.001$, ****: $p > 0.0001$. Scale bar = 20 μm.

(DOPE) were prepared by the sonication method.[45] DOTMA and DOPE were chosen as the carrier lipids due to their cationic/zwitterionic natures, which enhance attraction to the negatively charged cell membrane.[45] Liss-Rhod PE was included to enable tracking of the liposomes independent of the probe uncaging. Although a standard liposome formation method was initially attempted, significant optimization of buffer and lipid concentration was performed in order to circumvent the limited solubility of **PLP-ONOO⁻**. This can be rationalized by considering

that the parent DPPC headgroup is modified with the relatively hydrophobic butanone-coumarin motif, possibly decreasing the overall polarity of the molecule. The impact of different liposome compositions on the signal level and liposome incorporation into HeLa cells was assessed by incubating cells with liposomes prepared in cell-compatible medium (Hanks' Balanced Salt Solution, HBSS), then imaging by live cell confocal microscopy. We prepared liposomes of equimolar DOTMA/DOPE, in accordance with the literature precedence.[45] Preliminary results indicated that the amount of **PLP-ONOO$^-$** added affected both the fluorescence signal generation and the homogeneity of the liposomes. In particular, less than 4 mol% **PLP-ONOO$^-$** generated insufficient fluorescence signal upon probe uncaging. On the other hand, liposomes containing greater than 10 mol% **PLP-ONOO$^-$** were considerably more heterogenous in size (up to 20 μm observed, in contrast to ~100 nm) and nonuniform in vesicle lamellarity. To balance these counteracting factors, 4.5% probe was used, with 47.5% DOTMA and DOPE, each. The concentration of Liss-Rhod PE was kept constant at 0.5 mol% to minimize its impact on solubility and lipid dynamics. Liposomes comprised of Liss-Rhod PE/DOTMA/DOPE reached maximal incorporation into cells within 4 hours, however, for the liposomes containing **PLP-ONOO$^-$** the required incubation time increased to 12–18 hours. To accommodate this extended timeframe, liposomes were prepared in cell medium (Dulbecco's Modified Eagle Medium), instead of HBSS.

With a feasible liposome preparation and treatment protocol established, we then turned attention to assessing the cytocompatibility of the liposomal cargo, including **PLP-ONOO$^-$**, and the peroxynitrite-mediated oxidation products, **PLP*** and the oxa-spiro[4,5] decenone **6**. To this end, we employed a standard 3-(4,5-dimethylthiazol-2-yl)-2,5-diphenyl tetrazolium bromide (MTT) cell viability assay in HeLa cells treated with these molecules (8–250 μM) over a 24-hour period. The dose-response curves obtained from the MTT assay (Figure S7) provided high IC_{50} values (>100 μM) for the probe-containing liposomes, **PLP***, and **6** (Table S1). These results suggested that liposomes (50 μM) containing the probe or the oxidation products of the probe exhibit minimal cytotoxicity under our cell imaging conditions.

To acquire spatial information on HeLa cells, we employed the nucleic acid stain SYTO™ 9, as it possesses an excitation/emission profile not overlapping with that of either coumarin or rhodamine. Confocal microscopy of HeLa cells incorporating the liposomes revealed background coumarin fluorescence prior to peroxynitrite addition or stimulation, due either to the low-level intrinsic fluorescence of the caged probe or premature uncaging of the probe (Figure 3C, top panel). The background coumarin and Liss-Rhodamine signals overlapped, indicating

colocalization within the cell. The lipids showed no localization in the nucleus as indicated by no overlap with SYTO™ 9 stain. Upon treatment of the cells with 100 μM exogenous peroxynitrite, a significant increase in coumarin fluorescence was observed (Figure 3C, middle panel). This observation is consistent with the results obtained in the GV-based protocell membrane mimics. An order of magnitude lower concentration (10 μM) of exogenous peroxynitrite led to modest levels of intracellular fluorescence enhancement. This can be rationalized by considering the limited membrane permeability of peroxynitrite diffusing from an alkaline extracellular environment.

For a physiologically more relevant nitrosative stress model, we followed literature precedent to induce endogenous peroxynitrite production: stimulation of cells with IFN-γ and LPS, followed by PMA. IFN-γ/LPS treatment has been shown to lead to the production of NO through immunological stimulation, and PMA provokes increased levels of superoxide.[46] These two reactive species combine to form peroxynitrite, hence such conditions have been employed to stimulate peroxynitrite production intracellularly. Following stimulation, HeLa cells appeared morphologically diverse, and this was mirrored in the range of cellular probe fluorescence observed (Figure 3C, bottom panel). Most cells showed an increase in fluorescence compared to untreated cells, with a population that remained unchanged (Figure 3B).

Taken together, these results indicate that HeLa cells stimulated with either exogenous or endogenous peroxynitrite display significantly higher coumarin fluorescence compared to untreated cells. This difference can be observed qualitatively as brighter cyan signal in the $ONOO^-$ and LPS / IFN-γ / PMA images. Green (nucleic acid) and red (Liss-Rhod PE) signal intensity remains relatively stable following treatment, and thus can be used as subcellular localization markers.

CONCLUSION

In this work, we described the design and applications of a DPPC-derived peroxynitrite probe **PLP-ONOO⁻** for imaging lipid environments targeted by $ONOO^-$. Using this activity-based phospholipid and POPC, we built synthetic mimics of protocell membranes in the form of GVs. These GVs responded to $ONOO^-$ by lighting up at the membrane, remained physically intact, and showed excellent selectivity against other redox-active species. The lipid probe **PLP-ONOO⁻** was successfully incorporated into HeLa cells through liposomal uptake. Nitrosative stress, induced by either external administration of $ONOO^-$ or stimulation with IFN-γ/LPS/PMA,

resulted in fluorescence enhancement for primarily clustered lipids that are proximal to peroxynitrite. Further colocalization studies can be conducted with dyes specific for lipid-rich organelles, such as Golgi apparatus or endoplasmic reticulum. These studies would provide insight into i) which subcellular locations **PLP-ONOO$^-$** accumulates in and ii) which of those locations are susceptible to peroxynitrite.

Interest in expanding the chemical toolbox of synthetic lipids is surging and demand for applying these tools in both basic research and biomedicine is substantial.[47–49] Designer synthetic lipids have the ability to transform soft materials into biomimetic compartments with discrete functions.[50,51] This work, in particular, offers a platform for the development of lipid self-assemblies capable of sensing a chemical cue, offering a purely chemical perspective to cell-free biosensing.[52] In addition, our methodology enables investigation into the subcellular lipid environments that become targets of ONOO$^-$ during cellular nitrosative stress.

SUPPLEMENTARY INFORMATION

The Supplementary Information includes chemicals, methods and characterization for syntheses; method details for vesicle preparations; spectrophotometric measurements; cell viability assay; and supplementary figures.

ACKNOWLEDGMENT

We thank Dr. Ki-Bum Lee for allowing access to the fluorescence plate reader and we acknowledge Meiji Chen and Liming Wang for assistance with fluorescence assays.

FUNDING SOURCES

This work was supported by the US National Institutes of Health (NIH) / NIBIB Trailblazer Award (EB029548), the Rutgers Center for Lipid Research, the American Cancer Society, Institutional Research Grant Early Investigator Award, and the Rutgers Cancer Institute of New Jersey NCI Cancer Center Support Grant (P30CA072720).

AUTHOR CONTRIBUTIONS

E.C.I. conceived the study. B.G. and H.E. conducted the synthesis of the probes and spectroscopic and spectrophotometric analyses. B.G. established protocols for the preparation of giant vesicles. M.R.L.S. prepared the liposomes and performed the microscopy and cell work. T.A. performed pK_a measurement and MTT assay. All of the authors contributed to the

interpretation of data. E.C.I. wrote the manuscript with input from all authors. E.C.I. supervised the study.

DECLARATION OF INTEREST

The authors declare no competing interests.

REFERENCES

1. Fahy, E.; Cotter, D.; Sud, M.; Subramaniam, S. Lipid Classification, structure, and tools. *Biochimica. et Biophysica Acta*., 2011, 1811, 637-647.
2. Jackson, C.L.; Walch, L.; Verbavatz, J. Lipids and Their Trafficking: An Integral Part of Cellular Organization. *Cell. Dev. Rev.* 2016, *39*, 139–153.
3. Pennathur, S.; Jackson-Lewis, V.; Przedborski, S.; Heinecke, J.W. Mass Spectrometric Quantification of 3-nitrotyrosine, ortho-Tyrosine, and o,o'-Dityrosine in Brain Tissue of 1-Methyl-4-phenyl-1,2,3,6-tetrahydropyridine-treated Mice, a Model of Oxidative Stress in Parkinson's Disease. *J. Biol. Chem*., 1999, *274(49)*, 34621-34628.
4. Epe, B.; Ballmaier, D.; Roussyn, I.; Briviba, K.; Sies, H. DNA damage by Peroxynitrite characterized with DNA repair enzymes. *Nucleic Acids Res*., 1996, *24(21)*, 4105-4110.
5. Burney, S.; Caulfield, J.L.; Niles, J.C.; Wishnok, J.S., Tannenbaum, S.R. The chemistry of DNA damage from nitric oxide and peroxynitrite. *Mutat. Res.* 1999, *424*, 37–49.
6. Romero, N.; Radi, R.; Linares, E. Augusto, O.; Detweiler, C.D.; Mason, R.; Denicola, A. Reaction of Human Hemoglobin with Peroxynitrite Isomerization to Nitrate and Secondary Formation of Protein Radicals. *J. Biol. Chem*., 2003, *478(45)*, 44049-44057.
7. Radi, R., Oxygen radicals, nitric oxide, and peroxynitrite: Redox pathways in molecular medicine. *Proc. Natl. Acad. Sci.* 2018, *115*, 5839–5848.
8. Rubbo, H.; Trostchansky, A.; O'Donnell, V. Peroxynitrite-mediated lipid oxidation and nitration: mechanisms and consequences. *Arc. Biochem. Biophys.* 2009, *484*, 167–172.
9. D'Autréaux, B.; Toledano, M. B. ROS as signalling molecules: mechanisms that generate specificity in ROS homeostasis. *Nat. Rev. Mol. Cell Biol.* 2007, *8*, 813–824.
10. Holmström, K. M.; Finkel, T. Cellular mechanisms and physiological consequences of redox-dependent signalling. *Nat. Rev. Mol. Cell Biol.* 2014, *15*, 411–421.
11. Jiang, X.; Stockwell, B. R.; Conrad, M. Ferroptosis: mechanisms, biology and role in disease. *Nat. Rev. Mol. Cell Biol.* 2021, *22*, 266–282.
12. Cheung, E. C., Vousden, K. H. The role of ROS in tumour development and progression. *Nat. Rev. Cancer.* 2022, 1–18.
13. Szabo, C.; Ischiropoulos, H.; Radi, R. Peroxynitrite: biochemistry, pathophysiology and development of therapeutics. *Nat. Rev. Drug Discov.* 2007, *6*, 662–680.

14. Carballal, S.; Bartesaghi, S.; Radi, R. Kinetic and mechanistic considerations to assess the biological fate of peroxynitrite. *Biochim. Biophys. Acta.* 2014, *1840*, 768–780.

15. Ferrer-Sueta, G.; Radi, R., Chemical biology of peroxynitrite: kinetics, diffusion, and radicals. *ACS Chem. Biol.* 2009, *4*, 161–177.

16. Roots, R.; Okada, S. Estimation of life times and diffusion distances of radicals involved in X-ray-induced DNA strand breaks or killing of mammalian cells. *Radiat. Res.* 1975, *64*, 306–320.

17. Marla, S.; Lee, J.; Groves, J. Peroxynitrite rapidly permeates phospholipid membranes. *Proc. Natl. Acad. Sci.* 1997, *94*, 14243–14248.

18. Squadrito, G.; Pryor, W. Oxidative chemistry of nitric oxide: the roles of superoxide, peroxynitrite, and carbon dioxide. *Free Radic. Biol. Med.* 1998, *25*, 392–403.

19. Perrin, R.J.; Woods, W.S.; Clayton, D.F.; George, J.M. Exposure to Long Chain Polyunsaturated Fatty Acids Triggers Rapid Multimerization of Synucleins. *J. Biol. Chem*., 2001, *276(45)*, 41958–41962.

20. Dawson, T.M.; Dawson, V.L. Molecular Pathways of Neurodegeneration in Parkinson's Disease. *Science*, 2003, *302*, 819-822.

21. Qiao, S.; Li, W.; Tsubouchi, R.; Haneda, M.; Murakami, K.; Yoshino, M. Involvement of peroxynitrite in capsaicin-induced apoptosis of C6 glioma cells. *Neuroscience Res.* 2005, *51*, 175–183.

22. Cobbs, C.S.; Samanta, M.; Harkins, L.E.; Gillespie, G.Y.; Merrick, B.A.; MacMillan-Crow, L.A. Evidence for Peroxynitrite-mediated modifications to p53 in human gliomas: possible functional consequences. *Arch. Biochem. Biophys.* 2001, *394,* 167–172.

23. Kulahava, T.A.; Semenkova, G.N.; Kvacheva, Z. B.; Cherenkevich, S.N.; Timoshenko, A. Effects of Peroxynitrite and lipopolysaccharide on mitotic activity of C6 glioma cells. *Neurosci. Lett*. 2006, *398*, 286–290.

24. Pacher P, Schulz R, Liaudet L, Szabo C. Nitrosative stress and pharmacological modulation of heart failure. *Trends Pharmacol. Sci.* 2005, *26*, 302–310.

25. Pacher, P.; Beckman, J. S.; Liaudet, L. Nitric oxide and peroxynitrite in health and disease. *Physiol. Rev.* 2007, *87*, 315–424.

26. Wang, F.; Yuan, Q.; Chen, F.; Pang, J.; Pan, C.; Xu, F.; Chen, Y. Fundamental Mechanisms of the Cell Death Caused by Nitrosative Stress. *Front. Cell Dev. Biol*. 2021*, 9*, 1–9.

27. Yang, D.; Wang, H.-L.; Sun, Z.-N.; Chung, N.-W.; Shen, J.-G., A highly selective fluorescent probe for the detection and imaging of peroxynitrite in living cells. *J. Am. Chem. Soc.* 2006, *128*, 6004–6005.

28. Sun, Z.-N.; Wang, H.-L.; Liu, F.-Q.; Chen, Y.; Tam, P. K. H.; Yang, D. DODIPY-based fluorescent probe for Peroxynitrite detection and imaging in living cells. *Org. Lett.* 2009, *11*, 1887–1890.

29. Zhang, Q.; Zhu, Z.; Zheng, Y.; Cheng, J.; Zhang, N.; Long, Y. A Three-Channel Fluorescent Probe That Distinguishes Peroxynitrite from Hypochlorite. *J. Am. Chem. Soc*., 2012, *134*, 18479–18482.

30. Peng T.; Wong, N.; Chen, X.; Chan, Y.; Ho, D.H.; Sun, Z.; Hu, J.J.; Shen, J.; El-Nezami, H.; Yang, D. Molecular Imaging of Peroxynitrite with HKGreen-4 in Live Cells and Tissues. *J. Am. Chem. Soc.* 2014, *136*, 11728−11734.

31. Sun Y.; Dong, B.; Lu, Y.; Song, W.; Mehmood A. H.; Lin, W. A sensitive and selective fluorescent probe for the detection of endogenous Peroxynitrite ($ONOO^-$) in living cells. *Anal. Methods.* 2020, *12*, 2841–2845.

32. Sun, Q.; Xu, J.; Ji, C.; Shaibani, M.S.S.; Li, Z.; Lim, K.; Zhang, C.; Li, L.; Liu, Z. Ultrafast Detection of Peroxynitrite in Parkinson's Disease Models Using a Near-Infrared Fluorescent Probe. *Anal. Chem.* 2020, *92*, 4038–4045.

33. Gu, B.; Liu C.; Wu, Y.; Zhang, C.; Shen, Y.; Liu, M. Application of a Colorimetric and Near-Infrared Fluorescent Probe in Peroxynitrite Detection and Imaging in Living Cells. *ACS Omega* 2020, 5, *42*, 27530–27535.

34. Liu X.; Gu, F.; Zhou, X.; Zhou, W.; Zhang, S.; Cui, L.; Guo, T. A naphthalimide-based turn-on fluorescence probe for Peroxynitrite detection and imaging in living cells. *RSC Adv*. 2020, *10*, 38281–38286.

35. Zhang, J.; Zhen, X.; Zeng, J.; Pu, K. A Dual-Modal molecular probe for Near-Infrared Fluorescence and photoacoustic imaging of Peroxynitrite. *Anal. Chem*. 2018, *90*, 9301−9307.

36. Feng, S.; Zheng, Z.; Gong, S.; Feng, G. A unique probe enables labeling cell membrane and Golgi apparatus and tracking Peroxynitrite in Golgi oxidative stress and drug-induced liver injury. *Sensors and Actuators: B. Chem*. 2022, *261*, 131751, 1–11.

37. Reynolds, G.A.; Drexhage, K.H. New coumarin dyes with rigidized structure for flashlamp-pumped dye lasers. *Optics Commun.,* 1975, *13*, 222–225.

38. Alvarez, M. N., Piacenza, L., Irigoin, F., Peluffo, G. & Radi, R. Macrophage-derived peroxynitrite diffusion and toxicity to *Trypanosoma cruzi*. *Arch. Biochem. Biophys*. 2004, *432*, 222–232.

39. Cho, E., and Lu, Y. Compartmentalizing Cell-Free Systems: Toward Creating Life-Like Artificial Cells and Beyond. *ACS Synth. Biol.* 2020, *9*, 2881−2901.

40. Sezgin, E.; Levental, L.; Mayor, S.; Eggeling C. The mystery of membrane organization: composition, regulation, and roles of lipid rafts. *Nat. Rev. Mol. Cell. Bio.* 2017, *18*, 361-374.

41. Kurihara, K.; Okura, Y.; Matsuo, M.; Toyota, T.; Suzuki, K.; Sugawara, T. A Recursive Vesicle-Based Model Protocell with a Primitive Model Cell Cycle. *Nat. Commun.* 2015, *6*, 8352.

42. Weiss, M.; Frohnmayer, J. P.; Benk, L. T.; Haller, B.; Janiesch, J.- W.; Heitkamp, T.; Börsch, M.; Lira, R. B.; Dimova, R.; Lipowsky, R.; Bodenschatz, E.; Baret, J.-C.; Vidakovic-Koch, T.; Sundmacher, K.; Platzman, I.; Spatz, J. P. Sequential bottom-up assembly of mechanically stabilized synthetic cells by microfluidics. *Nat. Mater.* 2017, *17*, 89.

43. Göpfrich, K.; Haller, B.; Staufer, O.; Dreher, Y.; Mersdorf, U.; Platzman, I.; and Spatz, J. P. One-Pot Assembly of Complex Giant Unilamellar Vesicle-Based Synthetic Cells. *ACS Synth. Biol.* 2019, *8*, 937−947.

44. Stein, H.; Spindler, S.; Bonakdar, N.; Wang, C.; Sandoghdar, V. Production of isolated giant unilamellar vesicles under high salt concentrations. *Front. Physiol.* 2017, 8, 63.

45. Felgner, P.L.; Gadek, T.R.; Holm, M.; Roman, R.; Chan, H.W.; Wenz, M.; Northrop, J. P.; Ringold, G.M.; Danielsen, M. Lipofection: a highly efficient, lipid-mediated DNA-transfection procedure. *Proc. Natl. Acad. Sci. USA.* 1987, 84(21), 7413–7417.

46. Pfeiffer, S.; Lass, A.; Schmidt, K.; Mayer, B. Protein tyrosine nitration in cytokine-activated murine macrophages: involvement of a peroxidase/ nitrite pathway rather than Peroxynitrite. *J. Biol. Chem.* 2001, *276*, 34051–34058.

47. Klymchenko, A. S.; Kreder, R. Fluorescent probes for lipid rafts: From model membranes to living cells. *Chem. Biol.* 2014, *21*, 97− 113.

48. Flores, J.; White, B. M.; Brea, R. J.; Baskin, J. M.; Devaraj, N. K. Lipids: chemical tools for their synthesis, modification, and analysis. *Chem. Soc. Rev.* 2020, *49*, 4602-4614.

49. Mukhopadhyay, T. K.; Morstein, J.; Trauner, D., Photopharmacological control of cell signaling with photoswitchable lipids. *Curr. Opin. Pharmacol.* 2022, *63*, 102202.

50. Izgu, E. C.; Bjorkbom, A.; Kamat, N. P.; Lelyveld, V. S.; Zhang, W.; Jia, T. Z.; Szostak, J. W., *N*-carboxyanhydride-mediated fatty acylation of amino acids and peptides for functionalization of protocell membranes. *J. Am. Chem. Soc.* 2016, *138*, 16669–16676.

51. Lyu, Y.; Peng, R.; Liu, H.; Kuai, H.; Mo, L.; Han, D.; Li, J.; Tan, W. Protocells programmed through artificial reaction networks. *Chem. Sci.* 2020, *11*, 631−642.

52. Boyd, M. A.; Kamat, N. P. Designing Artificial Cells towards a New Generation of Biosensors. *Trends Biotechnol.* 2021, *39*, 927–939.